Environmental Science Nano

ROYAL SOCIETY OF CHEMISTRY

PAPER

View Article Online
View Journal | View Issue

Cite this: *Environ. Sci.: Nano*, 2026, 13, 895

Unravelling the effect of non-metal doping on polymeric carbon nitride for enhanced degradation of broad-spectrum antibiotics under visible light

Debanjali Dey,[a] Shamik Chowdhury *[b] and Ramkrishna Sen*[a]

Received 18th August 2025,
Accepted 8th January 2026

DOI: 10.1039/d5en00771b

rsc.li/es-nano

Advanced oxidation processes, such as heterogeneous photocatalysis, offer a green pathway for eliminating refractory organic pollutants. Despite notable advancements in photocatalyst design, limitations such as poor light-harvesting efficiency and fast electron–hole recombination remain significant bottlenecks for real-world deployment. To circumvent these shortcomings, herein, non-metal (B, S, P, and F) doped graphitic carbon nitride (GCN) was prepared *via* solid-state polycondensation of melamine with appropriate precursors of the respective dopants showcasing its superiority over conventional photocatalysts in degrading two representative broad-spectrum antibiotics, namely ofloxacin (OFC) and sulfamethoxazole (SMZ). The successful incorporation of non-metal dopants (B, S, P, and F) into the GCN framework was confirmed by a series of microscopic, spectroscopic, optical, and electrochemical characterization. The maximum degradation of antibiotics (98.9% for OFC and 96.6% for SMZ) was achieved using F-doped g-C_3N_4 (F-GCN) within 90 min of visible light illumination, primarily facilitated by holes and superoxide radicals. Although F-doping did not significantly enhance the photon absorption capacity of the GCN sample, the marked improvement in photocatalytic performance was clearly attributed to more efficient charge separation and migration. These findings coherently suggest that incorporating non-metal dopants can effectively enhance charge separation, making it a promising strategy for improving photocatalyst efficiency. To further validate the practical applicability of the F-GCN photocatalyst for water and wastewater treatment, its performance in removing a pharmaceutical cocktail from diverse aqueous matrices was evaluated. Comprehensive toxicity assessments of the photocatalytic degradation by-products, using bacterial colony counting and seed germination tests, confirmed the ecological safety of the treated antibiotic solution. Moreover, F-GCN exhibited remarkable reusability and photostability, underscoring its strong potential for large-scale photocatalytic wastewater treatment.

Environmental significance

The pervasive presence of antibiotics in aquatic environments is a growing global concern, as it accelerates the development and spread of antimicrobial resistance (AMR)—a major threat to public health and ecosystem stability. Conventional wastewater treatment methods often fail to adequately remove these pharmaceutically active compounds due to their high chemical stability. This study demonstrates a sustainable and efficient photocatalytic approach using non-metal doped polymeric carbon nitride (GCN) materials for the visible-light-driven degradation of broad-spectrum antibiotics such as sulfamethoxazole (SMZ) and ofloxacin (OFC). By mitigating antibiotic pollution at the source, this work contributes to reducing selective pressure on microbial communities, thereby curbing the emergence of resistant bacterial strains and supporting the global fight against AMR for a healthier and safer planet.

1. Introduction

The widespread occurrence of pharmaceutically active compounds (PhACs) in aquatic environments poses a serious public health challenge.[1] Owing to their inherent chemical stability, most PhACs are highly resistant to degradation, making their removal from water extremely difficult, particularly under the stringent conditions of wastewater streams. Notably,

[a] *Department of Bioscience and Biotechnology, Indian Institute of Technology Kharagpur, West Bengal 721302, India. E-mail: rksen@bt.iitkgp.ac.in*
[b] *School of Environmental Science and Engineering, Indian Institute of Technology Kharagpur, West Bengal 721302, India. E-mail: shamikc@iitkgp.ac.in*

elevated concentrations of antibiotics in environmental compartments exert selective pressure on resident bacterial strains, compelling them to evolve diverse resistance mechanisms as survival strategies under antibiotic-rich conditions, thereby accelerating the emergence of antimicrobial resistance.[2] The demand for highly efficient and economically viable wastewater treatment technologies has therefore become more urgent than ever.

Among the available approaches, heterogeneous photocatalysis has garnered significant attention due to its ability to rapidly degrade micropollutants into harmless end products.[3–6] This appeal stems from its facile operation, cost-effectiveness, non-selective nature, waste-free process, and environmentally friendly nature. Numerous studies have demonstrated the successful application of semiconductor-based photocatalysts in eliminating organic contaminants.[7–9] In particular, metal-free polymeric semiconductors such as two-dimensional graphitic carbon nitride (GCN) stand out as an exceptional candidate owing to its eco-friendly nature, low-cost precursors, remarkable stability, and simple synthesis procedure.[10,11] However, the practical deployment of GCN is constrained by its narrow visible light absorption range, low specific surface area, and poor charge carrier separation efficiency.[12] To address these shortcomings, various strategies have been explored, including defect engineering, heteroatom doping, cocatalyst incorporation, morphology tuning, and the construction of heterojunction structures, among others.[13]

Among these approaches, elemental doping, particularly with non-metals, such as boron (B), fluorine (F), phosphorus (P), and sulfur (S), has proven highly effective in tuning the electronic structure, aligning the band gap, extending photon absorption, and enhancing charge transfer efficiency.[13–15] In addition, introducing foreign elements can modulate the local electron density of GCN, increase the number of active sites, and facilitate the adsorption and activation of GCN with the target reactants on its surface.[13] Furthermore, these dopant atoms can either occupy intrinsic voids within the GCN framework or substitute for carbon or nitrogen atoms in its lattice.[13]

Previous studies have revealed that compared to pristine GCN, P-doped GCN can induce strong n → π* electronic transitions, resulting in a reduced band gap and improved light-harvesting capacity due to modifications in its electronic structure.[16,17] Likewise, S-doping alters the intrinsic electronic structure of GCN and increases its specific surface area, thereby improving visible light absorption, enriching reactive sites, and enhancing catalytic performance.[18–21] Interestingly, B-doping has been shown to strengthen the oxygen (O_2) adsorption capacity of GCN, increasing the adsorption energy from −0.47 eV to −1.19 eV.[22] In this case, B atoms act as electron-trapping centers, transferring electrons to nitrogen (N) atoms through B–N bonds and subsequently to adsorbed O_2 molecules, thereby facilitating their activation. Moreover, the incorporation of B into the GCN framework enables electron transfer from the π-electron system through the vacant $2p_z$ orbital of B.[23] Additionally, since B possesses lower electronegativity than C and N, it enhances the polarization of the π-electron structure, consequently improving charge carrier mobility.[23] On the other hand, F is also considered a promising dopant due to its exceptionally high electronegativity, which enables it to attract electrons from the surrounding lattice and thereby increase the local charge density of GCN.[24,25] Because the atomic radius of F is larger than that of C and N, the GCN framework tends to form C–F single bonds rather than undergoing substitutional doping.[25] This bonding configuration significantly enhances electron–hole separation and promotes more efficient electron transfer to the photocatalyst surface, ultimately boosting photocatalytic activity, as widely reported in the literature.[26,27]

All the above findings indicate that doping GCN with non-metal elements is highly beneficial for enhancing its photocatalytic performance. Therefore, in this study, we systematically investigated the comparative effects of B-, S-, P-, and F-doped GCN on the photocatalytic degradation of broad-spectrum antibiotics. Various non-metal-doped GCN photocatalysts were synthesized *via* a simple and cost-effective thermal polycondensation method and subsequently characterized using state-of-the-art techniques. Ofloxacin (OFC) and sulfamethoxazole (SMZ) were selected as representative pharmaceutical pollutants to evaluate the photocatalytic degradation performance of the doped GCN materials under visible light irradiation, with particular emphasis on their potential for practical environmental applications.

2. Materials and methods

2.1 Materials

Ascorbic acid (AA) ($C_6H_8O_6$, 99%), ethanol (C_2H_5OH, >99.9%), isopropyl alcohol (IPA) (C_3H_8O, 70% in H_2O), melamine ($C_3H_6N_6$, 99%), ofloxacin (OFC; $C_{18}H_{20}FN_3O_4$, analytical grade), potassium iodide (KI, ≥99%), sodium azide (SA) (NaN_3, ≥99.5%), sodium hydroxide (NaOH, >90%), sulfamethoxazole (SMZ; $C_{10}H_{11}N_3O_3S$, analytical grade), 5,5-dimethyl-1-pyrroline-*N*-oxide (DMPO; $C_6H_{11}NO$, ≥97%), and 2,2,6,6-tetramethylpiperidine-1-oxyl (TEMPO) ($C_9H_{17}NO$, 95%) were purchased from Sigma-Aldrich. Acetonitrile (HPLC grade, 99.9%), ammonium dihydrogen phosphate ($(NH_4)H_2PO_4$, 99.99%), ammonium fluoride (NH_4F, ≥99.99%), boric acid (H_3BO_3, >99.5%), calcium nitrate tetrahydrate ($Ca(NO_3)_2.4H_2O$, 99%), disodium hydrogen phosphate (Na_2HPO_4, ≥99%), magnesium nitrate hexahydrate ($Mg(NO_3)_2.6H_2O$, 99%), orthophosphoric acid (H_3PO_4, ≥85 wt%), potassium phosphate dibasic (K_2HPO_4), potassium nitrate (KNO_3, >99%), sodium carbonate (Na_2CO_3, ≥99.5%), sodium chloride (NaCl, ≥99%), sodium nitrate ($NaNO_3$, ≥99%), sodium sulfate (Na_2SO_4, ≥99%), and thiourea (CH_4N_2S, 99.99%) were procured from Merck. Nutrient broth and nutrient agar were purchased from HiMedia. Deionized water was used in all the experiments.

2.2 Synthesis of GCN and its doped variants

GCN was prepared *via* the thermal polycondensation of melamine. Specifically, 5 g of melamine was placed in a covered

alumina crucible and heated in a muffle furnace under an air atmosphere from room temperature to 550 °C at a rate of 8 °C min^{-1}, where it was maintained for 4 h. The resulting yellow solid was ground with a mortar and pestle, washed with ethanol, and subsequently dried under vacuum at 80 °C. The GCN yield was approximately 1.75 ± 0.15 g, corresponding to approximately 35% relative to the starting melamine mass.

Following this, various non-metal-doped GCN samples were synthesized. P-GCN was prepared by dissolving 5 g of melamine in 100 mL of deionized water along with 0.35 g of ammonium dihydrogen phosphate. The mixture was magnetically stirred at 80 °C overnight and then dried at 60 °C to obtain a white crystalline solid. The dried product was ground in an agate mortar and pestle, followed by calcination in air with a heating rate of 8 °C min^{-1} up to 550 °C, maintained for 4 h. The obtained product was washed with ethanol and water, then dried. The yield of P-GCN was 1.9 ± 0.08 g, corresponding to approximately 35.5% based on the initial reactant mass.

For F-GCN, 0.35 g of ammonium fluoride and 5 g of melamine were dissolved in 100 mL of deionized water and magnetically stirred for 12 h. The mixture was then dried at 60 °C and ground into a fine powder, which was placed in a covered alumina crucible and calcined in air at a heating rate of 8 °C min^{-1} to 550 °C for 4 h in a muffle furnace. The resulting yellow powder (F-GCN) was washed several times with ethanol and water to remove impurities and then dried. The yield was 1.8 ± 0.09 g, corresponding to approximately 33% relative to the total input.

B-GCN was synthesized *via* dissolving 5 g of melamine and 0.35 g of boric acid in 100 mL deionized water, followed by overnight stirring at 80 °C. The resulting white mixture was dried and then heated in a muffle furnace in air at a rate of 8 °C min^{-1} up to 550 °C, where it was maintained for 3 h. The obtained product (B-GCN) was washed with ethanol and water to remove any residual boric acid and dried in an oven at 60 °C for 12 h. The yield of B-GCN was approximately 2.1 ± 0.12 g, corresponding to approximately ~39% of the total input.

Finally, S-GCN was synthesized by thoroughly grinding 6 g of melamine and 3 g of thiourea in an agate mortar and pestle. The homogenous mixture was placed in a covered alumina crucible and calcined in air at a heating rate of 8 °C min^{-1} up to 550 °C for 4 h. The resulting yellow powder (S-GCN) was collected and dried. The yield was 3.8 ± 0.14 g, corresponding to approximately 42% of the total input.

2.3 Characterization techniques

Field-emission gun scanning electron microscopy (FEG-SEM) was performed using a Zeiss 206 Merlin system (Zeiss Merlin, Germany), equipped with a GEMINI II electromagnetic/electrostatic objective lens and an INCA X-sight energy-dispersive X-ray spectroscopy (EDS) detector (Oxford Instruments, UK). X-ray diffraction (XRD) patterns were obtained on a Bruker D8-DISCOVER 2D diffractometer (Bruker Corporation, Germany) employing a Cu Kα radiation source (λ = 1.5418 Å). Nitrogen adsorption–desorption isotherms were measured at −196 °C using a Belsorp Max II sorption analyzer (MicrotracBEL Corp., Japan) after degassing the samples at 200 °C for 16 h. The specific surface area and pore size distribution were calculated by the Brunauer–Emmett–Teller and Barrett–Joyner–Halenda (BJH) methods, respectively. Fourier transform infrared (FTIR) spectra were recorded on a Bruker Alpha II spectrometer (Bruker Corporation, Germany). X-ray photoelectron spectroscopy (XPS) measurements were carried out using a PHI 5000 Versa Probe III system (ULVAC-PHI Inc., Japan). UV-visible diffuse reflectance spectra were collected in the 200–800 nm range using an Analytik Jena Specord® S-600 spectrophotometer (Analytik Jena AG, Germany) equipped with an integrating sphere. Photoluminescence (PL) spectra were acquired on an F-4600 fluorescence spectrometer (Horiba Jobin Yvon Inc., France) using an excitation wavelength of 368 nm. Electrochemical impedance spectroscopy (EIS) was conducted on a Metrohm Autolab PGSTAT204 workstation (Metrohm Autolab BV, Netherlands) in 1 mol L^{-1} potassium chloride using a three-electrode setup. For electrode preparation, 0.012 g of photocatalyst was ultrasonically dispersed in 8 mL of acetone and coated onto carbon felt to serve as the working electrode; a platinum plate and silver/silver chloride were used as the counter and reference electrodes, respectively. Reactive oxygen species (ROS) involved in the photocatalysis process was investigated *via* electron paramagnetic resonance (EPR) spectroscopy using an Elexsys E580 spectrometer (Bruker Corporation, Germany) using DMPO and TEMPO as spin-trapping agents. Zeta potential measurements were performed using a Zetasizer Nano ZS90 analyzer (Malvern PANalytical Ltd., Switzerland).

2.4 Photocatalytic experiments

The photocatalytic degradation of SMZ and OFC was carried out in a custom-designed batch-type photochemical reactor (Lelesil Innovative Systems, India). Illumination was provided *in situ* by a 250 W arc-type mercury vapor lamp, fitted with a UV cutoff filter (λ < 420 nm), exhibiting primary emission lines at ~468 nm (blue), ~500 nm (cyan), ~540 nm (green), and ~660 nm (red) (Fig. S1), and a luminous intensity of 470 × 10^2 l× and irradiance of 103.8 W m^{-2}. The incident photon flux was experimentally measured using Reinecke's salt actinometry, yielding a value of 4.83 × 10^{-4} Einstein m^{-2} s^{-1} (≈2.9 × 10^{20} photons m^{-2} s^{-1}). The lamp was centrally mounted within the reactor to ensure uniform light distribution. In a typical experimental run, 100 mL of an aqueous OFC or SMZ solution (10 mg L^{-1}) was placed in the reaction vessel, followed by the addition of 100 mg of catalyst. The suspension was stirred in the dark for 30 min to achieve the adsorption–desorption equilibrium. Subsequently, the system was exposed to visible light while maintaining a steady reaction temperature of 25 ± 2 °C. At regular intervals, aliquots were withdrawn to determine the OFC or SMZ concentration using an ultrahigh-performance liquid chromatography (UHPLC) system (UltiMate 3000, Thermo Fisher Scientific Inc., USA) fitted with a Hypersil GOLD

C18 column (4.6 × 250 mm^2). For SMZ quantification, acetonitrile (60% v/v) was used as the mobile phase, and detection was performed at 270 nm. For OFC quantification, isocratic elution was performed using potassium dihydrogen phosphate buffer (70% v/v; pH 3, adjusted with *o*-phosphoric acid) and acetonitrile (30% v/v) at a flow rate of 1 mL min^{-1}, with detection at 290 nm. The injection volume was 10 μL for both cases. All mobile phase solutions were degassed by sonication before use. The durability and reusability of the developed photocatalysts were assessed through successive reuse experiments.

To investigate the intermediate products formed during the photocatalytic degradation, filtered samples were analyzed using a liquid chromatography-mass spectrometry (LCMS) system (Waters 2695 XE separations module coupled with a Quattro Micro™ API mass spectrometer, Waters Corporation, USA). The total organic carbon (TOC) content after photocatalysis was measured using a TOC-L analyzer (Shimadzu Corp., Japan).

The toxicity of the photocatalysis end-products was further assessed against *Escherichia coli* (*E. coli*) using the standard plate count technique. Phytotoxicity was evaluated through germination and seedling growth assays using mung bean (*Vigna radiata*) seeds. The seeds were washed with deionized water, dried, and placed in vented Petri dishes lined with germination paper moistened with 5 mL of either untreated or treated OFC or SMZ solutions. Control seeds were moistened with deionized water and germinated under identical conditions. Germination was initiated in the dark for 48 h at 25 ± 2 °C, followed by a 3-day light–dark cycle. Toxicity was evaluated based on the germination index and measurements of shoot and root lengths following standard protocols.

To evaluate the real-world applicability of the synthesised materials, OFC, SMZ, carbamazepine (CBZ; $C_{15}H_{12}N_2O$, ≥98%, Sigma-Aldrich), and acetaminophen (ACT; $C_8H_9NO_2$, ≥99%, Sigma-Aldrich) were introduced into various real water matrices like tap water (TW), surface water (SW), municipal wastewater (MWW), and hospital wastewater (HWW). The TW sample was collected from a laboratory at the Indian Institute of Technology Kharagpur (West Bengal, India), and the SW sample was sourced from the Kangsabati river flowing near Kharagpur. Besides, HWW was obtained from the sewage system of a nearby hospital in Kharagpur, while MWW was sampled from the influent of a wastewater treatment plant in Kharagpur.

All experiments were conducted in triplicate, and the results are reported as mean ± standard deviation.

3. Results and discussion

3.1 Characterization of GCN and its doped variants

The purity and crystalline structure of pristine GCN and non-metal-doped GCN photocatalysts were examined using XRD, with the corresponding diffraction patterns shown in Fig. 1a. Two prominent peaks at 2θ values of 13.1° and 27.4° correspond to the (100) and (002) diffraction planes of bare GCN (JCPDS No. 87-1526). The intense peak at 27.4° (interlayer spacing 0.32 nm) is attributed to the interlayer stacking of conjugated aromatic structures, while the weaker peak at 13.1° (interlayer spacing 0.67 nm) is assigned to the in-plane structural packing of tri-*s*-triazine units. These two

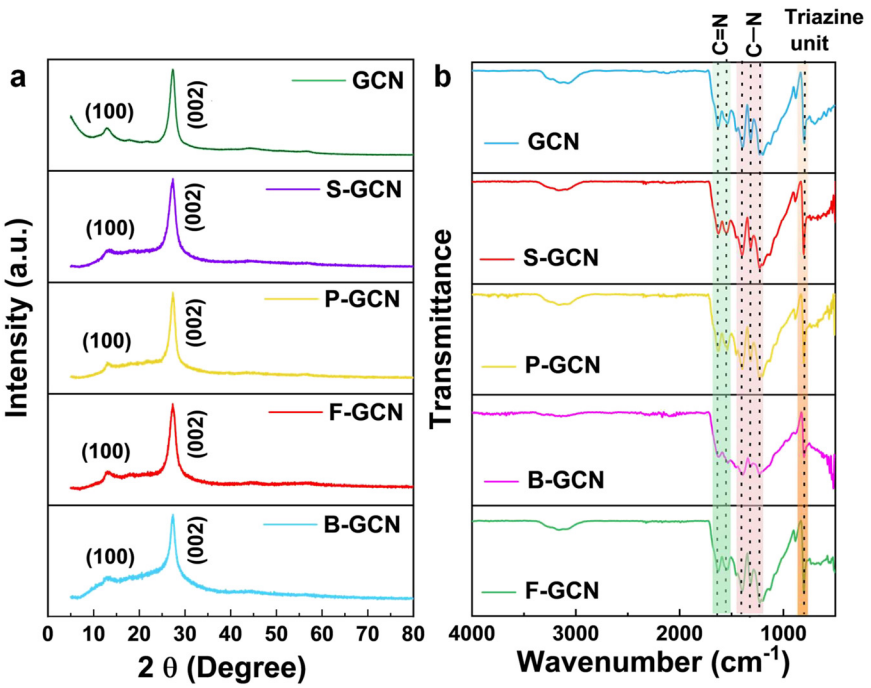

Fig. 1 (a) XRD patterns and (b) FTIR fingerprints of GCN, B-GCN, S-GCN, P-GCN, and FGCN.

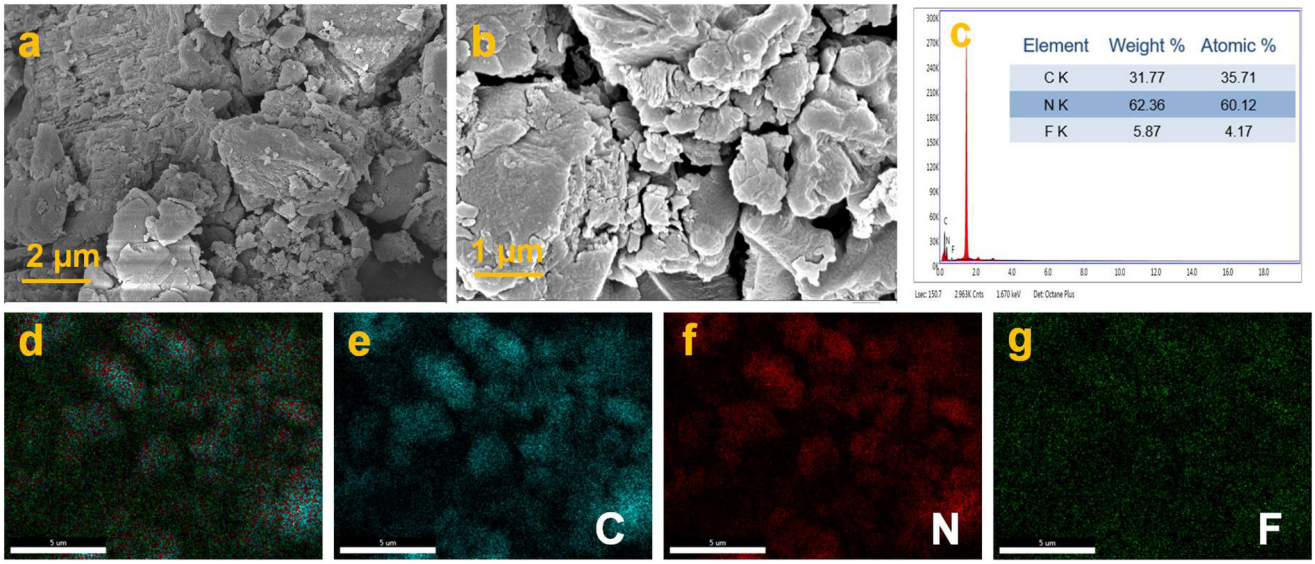

Fig. 2 FEG-SEM images of (a) GCN and (b) F-GCN. (c) EDS spectrum. (d) EDS overlay elemental map, and individual mappings of F-GCN for (e) carbon (C), (f) nitrogen (N), and (g) fluorine (F).

characteristic peaks are also observed in the XRD patterns of B-GCN, S-GCN, P-GCN, and F-GCN samples, indicating that the introduction of non-metal dopants did not alter the fundamental GCN framework. Furthermore, no additional peaks related to impurity phases were detected, and the sharp diffraction peaks confirmed both the purity and high crystallinity of the synthesized materials.

The surface chemical properties of GCN and non-metal-doped GCN were discerned with the aid of FTIR spectroscopy, revealing the characteristic IR fingerprints of F-GCN (Fig. 1b). The distinct band observed at 810 cm^{-1} is attributed to the bending vibration mode of the tri-*s*-triazine ring in GCN.[26] Additionally, the multiple bands appearing in the 1700–1200 cm^{-1} range are associated with the C–N and C═N stretching vibrations of the heterocyclic framework.[25] The broad absorption band between 3000 and 3500 cm^{-1} corresponds to the stretching vibrations of N–H and O–H bonds, originating from residual amine groups and surface-adsorbed moisture, respectively. Notably, the FTIR spectra showed no major changes after doping with non-metals (B, S, P, and F), although very minor shifts and differences in band sharpness were detected in certain regions compared to pristine GCN (Fig. 1b). These results suggest that B, S, P, and F were effectively incorporated into the GCN structure.

The morphology of pure GCN and F-GCN was examined *via* FEG-SEM. Pristine GCN exhibited an organized crystalline morphology with visible flakes and a lamellar structure (Fig. 2a). Similarly, F-GCN possessed a comparable layered morphology, indicating that F-doping has a negligible influence on the morphology of GCN (Fig. 2b). Moreover, the EDS elemental composition (Fig. 2c) and mapping images (Fig. 2d–g) of F-GCN endorse the presence of C, N, and F elements.

Further, XPS analysis was performed to determine the elemental valence states and examine the detailed chemical composition of the samples. The atomic percentages of C, N, O, and the respective dopant elements (F, B, S, and P), quantified from XPS survey spectra, are summarized in Table S1. The full survey spectra (Fig. 3a and b) for GCN and F-GCN revealed three distinct peaks at approximately 284, 398, and 530 eV, corresponding to C 1s, N 1s, and O 1s signals, respectively. The O 1s peaks can be attributed to adsorbed water or oxygen-containing uncondensed intermediates formed during the pyrolysis of melamine. Additionally, the F-GCN survey spectrum displayed a weak peak at around 684 eV, confirming the successful introduction of F dopants into the heptazine structure of GCN. In the C 1s spectrum of GCN (Fig. 3c), three distinct peaks are observed: one near 284.6 eV corresponding to graphitic C═C bonds, and two at approximately 286.3 and 288.1 eV attributed to C atoms in C–NH_2 and N═C–N bonds, respectively.[28,29] Likewise, the deconvoluted C 1s spectrum of F-GCN (Fig. 3d) displays three peaks at 283.3, 286.6, and 291.3 eV, assigned to graphitic C═C, C–NH_2, and semi-ionic C–F_2 bonds, respectively.[28–30] The high-resolution N 1s region of GCN (Fig. 3e) reveals a major peak centred at 398.6 eV,[31,32] corresponding to sp^2-hybridized N (C–N═C), while three minor peaks at 399.6, 400.6, and 404.4 eV are associated with bridging tertiary nitrogen atoms [N–$(C)_3$], uncondensed C–N–H side groups, and π-excitation, respectively.[29,33] In contrast, the N 1s spectrum of F-GCN (Fig. 3f) shows three peaks at approximately 398.61, 400.27, and 404.5 eV, attributed to C–N═C, C–N–H side groups, and π-excitation, respectively (Fig. 3f). For the F 1s region, a single peak centered at 684.1 eV is characteristic of C–F coordination (Fig. 3g). The presence of C–F bonding in the XPS spectra indicates that F is predominantly incorporated *via* surface functionalization and partial substitution at nitrogen-linked carbon sites in the GCN framework, rather than interstitial doping. These findings conclusively confirm the presence of F element within the GCN framework.

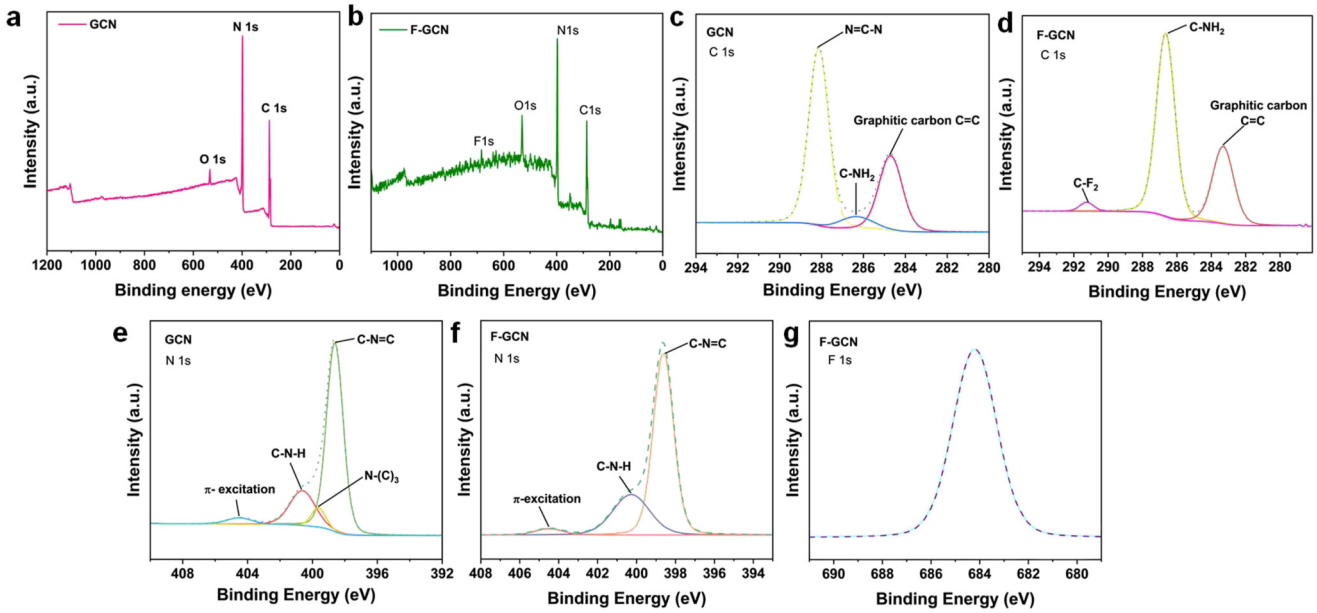

Fig. 3 XPS survey scan spectra of (a) GCN and (b) F-GCN. High resolution deconvoluted (c and d) C 1s and (e and f) N 1s spectra for GCN and F-GCN, respectively, and (g) F 1s spectrum of F-GCN.

The textural characteristics of the as-synthesized materials were assessed through N_2 adsorption–desorption isotherm measurements, as presented in Fig. 4a. All samples exhibited type IV isotherms with an H3 hysteresis loop. The pore size distribution, determined from the desorption branch data using the BJH method (Fig. 4b), revealed that most pores in GCN and non-metal-doped GCN fall within the mesoporous range. The mesoporous structure enhances photocatalytic performance by facilitating mass transfer and diffusion of reactant molecules. The specific surface area, pore volume, and average pore

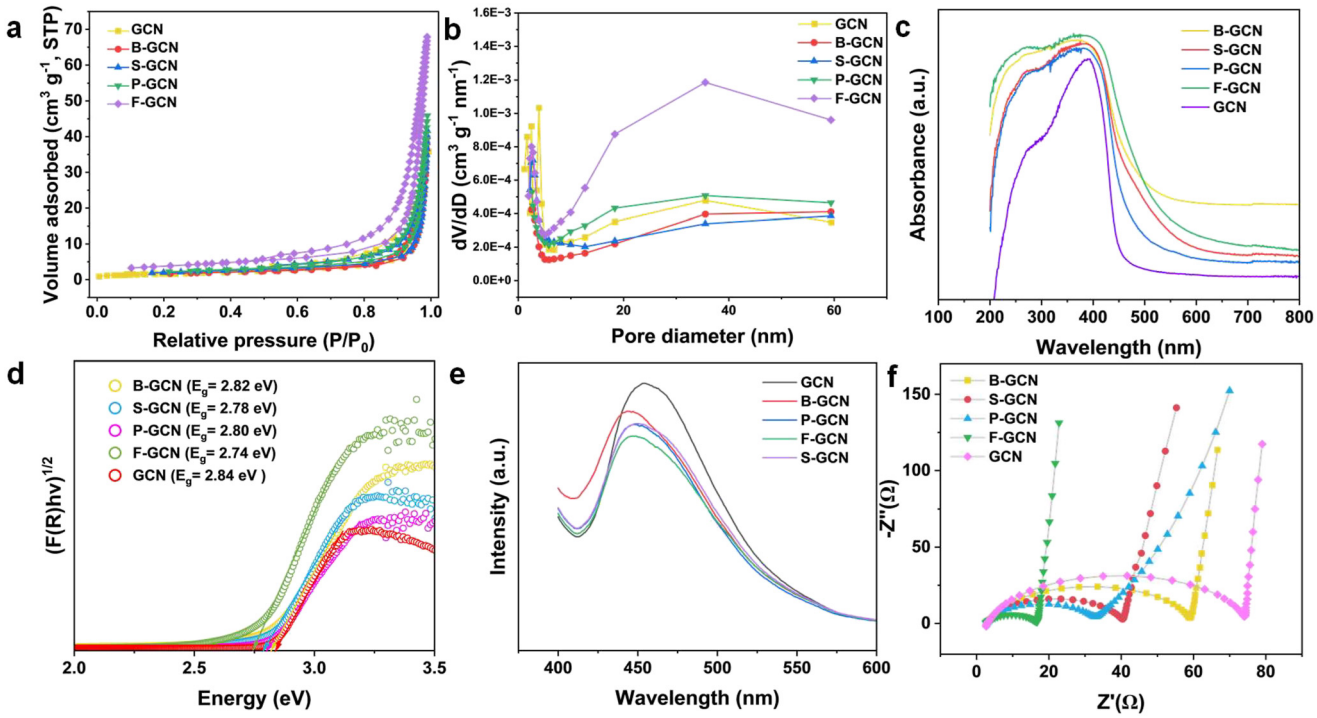

Fig. 4 (a) N_2 adsorption–desorption isotherms of GCN and non-metal doped GCN, measured volumetrically at −196 °C. (b) Pore size distribution curves of GCN and non-metal doped GCN. (c) UV-vis diffuse reflectance spectra and (d) Kubelka–Munk plots for band gap estimation of GCN and non-metal doped GCN. (e) Steady-state PL spectra and (f) EIS spectra of GCN and non-metal doped GCN.

diameter of all the samples are listed in Table S2. Notably, F-GCN exhibits a significantly higher specific surface area (13 m^2 g^{-1}) and pore volume (0.102 cm^3 g^{-1}), in comparison to pristine GCN, while maintaining a mesoporous structure (~35.3 nm), which improves both pollutant adsorption and mass transfer-assisted photocatalytic degradation of organic pollutants.

The optical properties of the synthesized samples were examined using UV-visible diffuse reflectance spectra. As shown in Fig. 4c, all photocatalysts exhibited light absorption from the UV region into the visible range (>460 nm), with the absorption edge of pristine GCN observed at approximately 410 nm. Compared with GCN, the light absorption of B-GCN, S-GCN, P-GCN, and F-GCN was enhanced in both UV and visible light regions. The optical band gap energies (E_g) were estimated from UV-vis diffuse reflectance spectra using the Kubelka–Munk function, $F(R_\infty) = (1 - R_\infty)^2/(2R_\infty)$. Considering that GCN is an indirect semiconductor, the band gaps were determined using the indirect allowed transition model by plotting $[F(R_\infty)h\nu]^{1/2}$ as a function of photon energy ($h\nu$) where R_∞ (= $R_{sample}/R_{standard}$) is the reflectance of an infinitely thick specimen, h is the Plank constant (6.63×10^{-34} J s) and ν is the photon frequency. The E_g values were obtained by extrapolating the linear portion of the plots to the energy axis. The E_g values, as determined *via* Kubelka–Munk plots (Fig. 4d), are 2.84, 2.82, 2.80, 2.78, and 2.74 eV for GCN, B-GCN, P-GCN, S-GCN, and F-GCN, respectively. These results indicate that doping with non-metals, such as B, P, S, and F, does not significantly alter the band gap of GCN.

The influence of non-metal doping on the recombination rate and efficiency of photogenerated charge carrier separation in GCN was assessed using PL analysis. A lower PL intensity generally indicates slower recombination and more effective charge separation. PL spectra for all samples were recorded at an excitation wavelength of 368 nm, as shown in Fig. 4e. Pristine GCN exhibited a strong emission peak at 460 nm, attributed to the rapid recombination of photogenerated charge carriers. In contrast, B-, S-, P-, and F-doped GCN samples displayed significantly lower PL intensities, suggesting improved charge separation and longer carrier lifetimes due to non-metal incorporation. Among them, F-GCN exhibited the lowest PL signal, likely due to the strong electronegativity of F, which acts as surface trapping sites for photogenerated carriers, thereby reducing recombination rates and ameliorating the overall photocatalytic performance.

Additionally, EIS-based Nyquist plots are widely recognized as reliable indicators of charge carrier migration and interfacial transfer/recombination rates. As illustrated in Fig. 4f, the non-metal-doped GCN samples demonstrated reduced electrical resistance compared to pure GCN, which is evidenced by their smaller Nyquist arc radii, indicating improved charge transport capabilities. Notably, the Nyquist arc radius of F-GCN is the smallest among all samples, signifying more efficient photogenerated charge carrier separation, superior electrical conductivity, and enhanced interfacial charge mobility.

3.2 Photocatalytic degradation of antibiotics

The photocatalytic activity of pure GCN and non-metal-doped GCN catalysts was evaluated by investigating the degradation of two broad-spectrum antibiotics, OFC and SMZ, as shown in Fig. 5a and b. The adsorption extent of both the antibiotics was invariably low and reached adsorption–desorption equilibrium within 30 min during the dark adsorption phase (Fig. S2). Therefore, prior to illumination, the antibiotic–photocatalyst suspension was magnetically stirred in the dark for 30 min across all experiments. Subsequently, the photocatalytic performance was assessed based on the visible light-driven degradation of OFC and SMZ. In the absence of the photocatalyst, only about 12% OFC and 10.5% SMZ were degraded after 90 min of irradiation, indicating that direct photolysis is relatively ineffective in breaking down the antibiotic pollutants. In contrast, all the non-metal-doped GCN samples exhibited significantly enhanced photocatalytic activity compared to pristine GCN, demonstrating the beneficial effect of heteroatom incorporation on charge separation and visible light utilization. Since the doping content on GCN is nearly comparable, it is reasonable to compare the photocatalytic activity of various non-metal-doped GCN photocatalysts. Among them, F-GCN exhibits the highest photocatalytic activity, achieving degradation efficiencies of 98.9% for OFC and 96.5% for SMZ, compared to pristine GCN (88.7% for OFC and 85.8% for SMZ). The performance decreases in the order: F-GCN > P-GCN (96.6% for OFC and 93.2% for SMZ) > S-GCN (95.0% for OFC and 92.0% for SMZ) > B-GCN (92.7% for OFC and 89.0% for SMZ). Notably, F-GCN, which possesses the largest specific surface area and the lowest band gap, demonstrates the highest photocatalytic activity among all the samples. Furthermore, F-GCN exhibits a high content of semi-ionic C–F bonds, whose strong polarization induces local electronic redistribution and promotes effective separation of photogenerated charge carriers, thereby enhancing photocatalytic performance. Moreover, F-doping is known to introduce defect states and surface vacancies, providing shallow trapping sites that suppress electron–hole recombination. These polarized bonds and defect-rich domains also improve interfacial charge transfer by strengthening interactions between the photocatalyst surface and reactant molecules. Consequently, the synergistic effects of bond polarization, defect-mediated charge trapping, and enhanced interfacial charge transfer collectively contribute to the superior photocatalytic activity observed for F-GCN relative to other doped GCN systems.

Moreover, the apparent rate constants (k) for the degradation of OFC and SMZ, calculated using the traditional Langmuir–Hinshelwood kinetic model based on the experimental data, follow the same decreasing trend for OFC (Fig. 5c) and SMZ (Fig. 5d) as observed in the photocatalytic degradation results. Although GCN and its non-metal-doped counterparts possess comparable band gap energies, pristine GCN exhibits markedly lower photocatalytic activity than F-GCN for the degradation of both antibiotics. The superior photocatalytic activity of F-GCN, compared with pristine GCN and other doped samples, can be

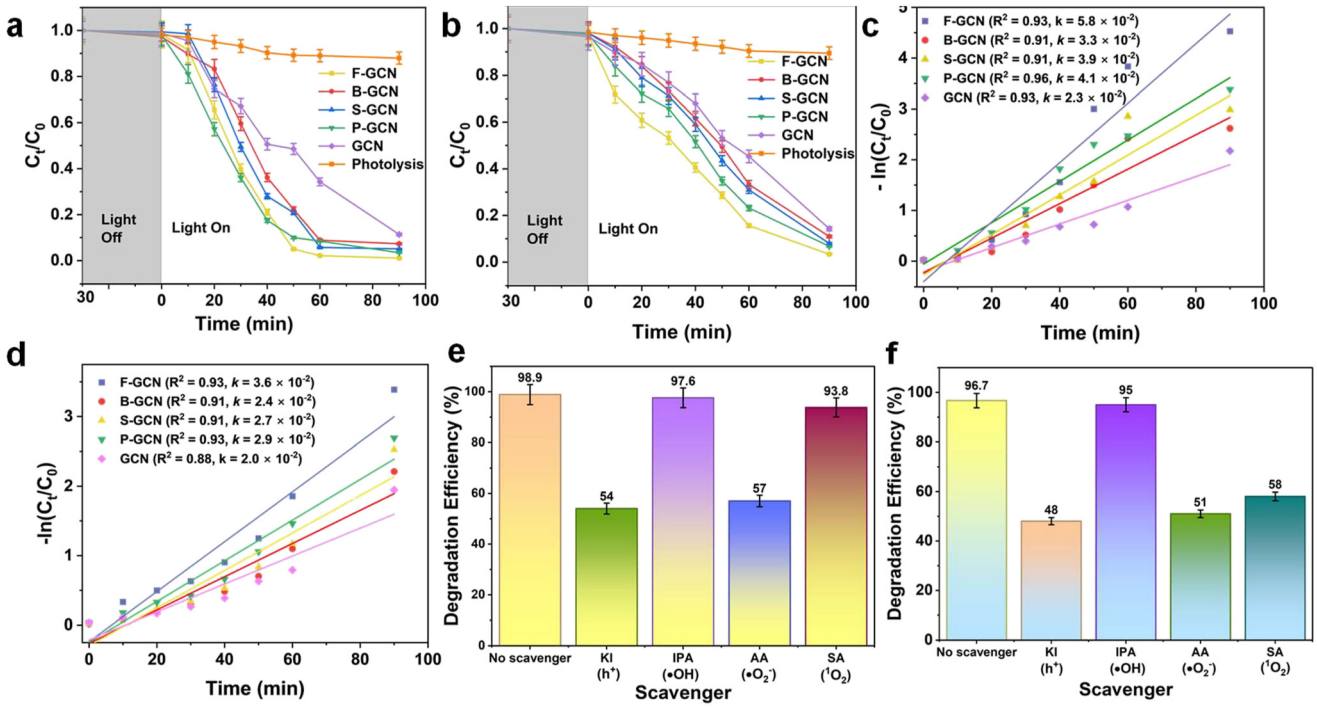

Fig. 5 Visible light-induced photocatalytic degradation of (a) OFC and (b) SMZ over GCN and non-metal doped GCN. Langmuir–Hinshelwood kinetic plots for the degradation of (c) OFC and (d) SMZ under the same conditions (experimental conditions: initial concentration of the antibiotic = 10 mg L^{-1}; photocatalyst dosage = 1 g L^{-1}; temperature = 25 ± 2 °C). Photocatalytic degradation of (e) OFC and (f) SMZ in the presence and absence of ROS scavengers and hole quencher (experimental conditions: photocatalyst dosage = 1 g L^{-1}; C_0 = 10 mgL^{-1}; scavenger = 20 mM; temperature = 25 ± 2 °C).

attributed to the unique influence of F on the physicochemical and electronic structures of GCN. Unlike non-metal dopants such as B or P, which primarily act as electron donors and modify the electronic band positions, F induces localized polarization within the GCN framework owing to its strong electronegativity. This polarization enhances charge carrier separation by creating internal dipole moments and facilitating faster electron migration to the surface. In addition, the partial substitution of N atoms with F leads to the formation of C–F bonds that passivate surface defects and suppress charge recombination. Moreover, when compared with S-doping, which typically narrows the band gap but introduces mid-gap states that promote recombination, F-doping achieves a balanced band structure that maintains strong visible light absorption while preserving efficient charge transport. The resultant optimized band positions of F-GCN favor both the generation and transfer of photogenerated electron–hole pairs, leading to markedly higher photocatalytic degradation rates. These synergistic effects confirm that F plays a more effective role than B, S, or P in improving the photocatalytic efficiency and stability of GCN under visible light. Notably, after 90 min of treatment with F-GCN, the TOC removal reached 82.3% for OFC and 78.5% for SMZ (Fig. S3), underscoring the high efficiency of this photocatalyst in achieving pollutant mineralization. Furthermore, as shown in Table S3, F-GCN exhibits significantly superior photocatalytic performance and degradation rates compared with many previously reported photocatalysts, as discussed in Text S1 (see SI).

To identify the contribution of different ROS, including superoxide anions ($^{\bullet}O_2^-$), hydroxyl radicals ($^{\bullet}OH$), singlet oxygen ($^1O_2$), and photogenerated holes (h^+), photocatalytic reactions were performed in the presence of specific quenchers (20 mmol L^{-1} each): AA for $^{\bullet}O_2^-$, SA for $^1O_2$, IPA for $^{\bullet}OH$, and KI for h^+. Compared to the photocatalytic activity without any scavenger, the addition of KI and AA led to the most pronounced decline in removal efficiency for both antibiotics. As shown in Fig. 5e and f, the degradation efficiency decreased to 54% for OFC and 48% for SMZ with KI, and to 57% for OFC and 51% for SMZ with AA. These results clearly indicate that h^+ and $^{\bullet}O_2^-$ are the predominant reactive species responsible for the photocatalytic degradation of OFC and SMZ. While $^1O_2$ exhibited only a minor effect on OFC degradation (93.8%), it played a more significant role in the degradation of SMZ (58%). In contrast, the addition of IPA had no noticeable inhibitory effect on the degradation of either antibiotic. This conclusion is further supported by EPR spectroscopy, which reveals intense signals corresponding to the DMPO–$^{\bullet}O_2^-$ adduct and the TEMPO–hole complex under visible light irradiation of the F-GCN suspension (Fig. S4a and b), thereby confirming that $^{\bullet}O_2^-$ and h^+ are indeed the primary reactive species involved.

3.2.1 Photocatalytic mechanism of antibiotic degradation. In accordance with the above findings and discussion, a reaction mechanism for antibiotic degradation using the F-GCN photocatalyst is proposed, as illustrated in Fig. 6b. As deduced from the Kubelka–Munk plot, the E_g of F-GCN is calculated to

be 2.74 eV (Fig. 4d). As shown in Fig. 6a, the flat-band potential (V_{fb}) of F-GCN is determined to be −0.74 V (*vs.* standard hydrogen electrode, SHE). Further, the Mott–Schottky plot of F-GCN exhibits a positive slope, confirming its n-type semiconductor nature. For n-type semiconductors, the conduction band (CB) potential (E_{CB}) is typically 0.1–0.2 V more negative than the flat-band potential (V_{fb}).[34,35] Accordingly, the E_{CB} of F-GCN is enumerated as −0.94 V. Subsequently, the valence band (VB) potential (E_{VB}) of F-GCN is estimated to be 1.8 V, based on the empirical formula $E_{VB} = E_{CB} + E_g$. Based on these band positions, F-GCN is well-positioned to drive the formation of ROS under visible light irradiation. Upon light irradiation of F-GCN, photogenerated charge carriers are separated (eqn (1)). Since, the E_{CB} of F-GCN (−0.94 V) is more negative than the standard redox potential of $O_2/{}^{\bullet}O_2^-$ (−0.33 V),[36,37] oxygen molecules adsorbed on the F-GCN surface can readily accept photoexcited electrons from the CB, forming ${}^{\bullet}O_2^-$ species that subsequently participate in the oxidation of antibiotic pollutants. Additionally, the direct hole-mediated oxidation of OFC and SMZ proceeds simultaneously with the formation of ${}^{\bullet}O_2^-$ radicals, and both pathways collectively contribute to the production of intermediate degradation products. Furthermore, some ${}^{\bullet}O_2^-$ radicals are oxidized by VB holes, producing $^1O_2$,[33,36] which further promotes the breakdown of antibiotics into smaller intermediates. The series of plausible reactions outlining this photocatalytic process is summarized in eqn (2)–(6):

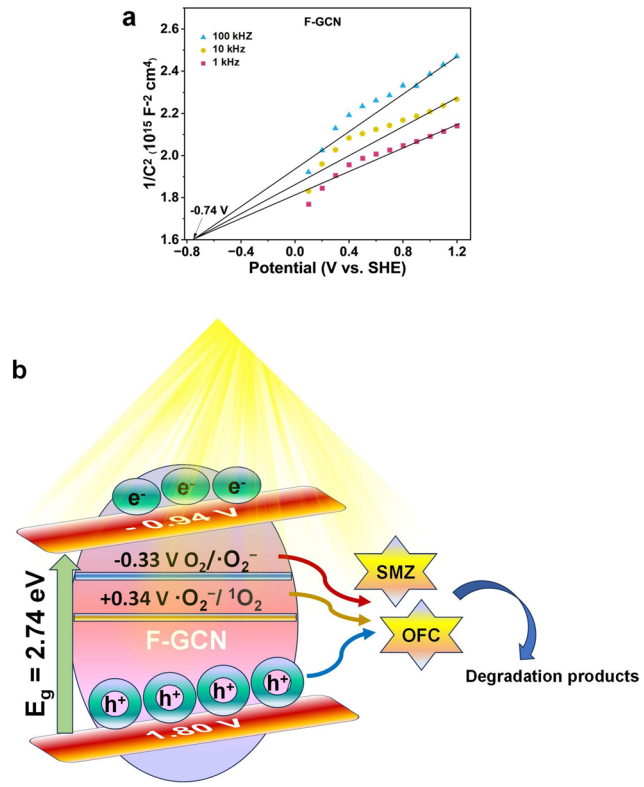

Fig. 6 (a) Mott–Schottky plots of F-GCN measured at three different frequencies. (b) Schematic of the proposed mechanism for antibiotic degradation over F-GCN under visible light irradiation.

$$\text{F-GCN} + h\nu\ (\text{light}) \rightarrow \text{F-GCN}\ (h^+ + e^-) \quad (1)$$

$$O_2 + e^- \rightarrow {}^{\bullet}O_2^- \quad (2)$$

$${}^{\bullet}O_2^- + h^+ \rightarrow {}^1O_2 \quad (3)$$

$$h^+ + \text{OFC/SMZ} \rightarrow \text{degradation products} \quad (4)$$

$${}^{\bullet}O_2^- + \text{OFC/SMZ} \rightarrow \text{degradation products} \quad (5)$$

$${}^{\bullet}O_2 + \text{OFC/SMZ} \rightarrow \text{degradation products} \quad (6)$$

3.2.2 Effect of operational parameters

Effect of pH. The influence of environmental factors on the F-GCN photocatalyst was systematically investigated. Among these, the initial solution pH is a critical parameter, governing the protonation of surface functional groups and, consequently, significantly affecting the degradation efficiency of waterborne pollutants. To explore this effect, the zeta potential of F-GCN was measured across a wide pH range, revealing a point of zero charge (pHpzc) near 4.3 (Fig. 7a). Meanwhile, the OFC molecule (pK_{a1} = 5.97, pK_{a2} = 8.3) primarily exists in its cationic form at pH 3 and 5. At pH 3, electrostatic repulsion between OFC^+ and positively charged F-GCN results in a lower degradation efficiency of 95.9% (Fig. 7b). As the pH increases to 5, electrostatic attraction between OFC^+ and negatively charged F-GCN enhances degradation. The highest photocatalytic performance (99%) is observed at neutral pH, where strong electrostatic interactions between neutral OFC^0 and negatively charged F-GCN facilitate efficient degradation. At pH values above 8.3, the predominance of OFC^- leads to electrostatic repulsion with F-GCN particles, causing a slight decline in photocatalytic efficiency.

For SMZ, efficient dissociation occurs primarily within the pH range of 3 to 7, compared to more alkaline conditions (Fig. 7c). SMZ, with pK_{a1} = 1.6 and pK_{a2} = 5.7, exists as a zwitterion between pH 1.6 and 5.7, and as an anion at pH > 5.7. At pH 3, electrostatic attraction between positively charged F-GCN and the zwitterionic SMZ^0 leads to the highest degradation (99.7% within 60 min). At pH 5, a strong attraction between negatively charged F-GCN and the positively charged domains of SMZ^0 results in substantial degradation (98% within 90 min). Although SMZ^- dominates at pH > 5.7, the degradation efficiency at pH 7 remains high (96.7%), likely due to negative charge-assisted hydrogen bonding between anionic SMZ^- (H-donors) and nitrogen-containing groups on F-GCN (H-acceptors). Conversely, at pH values above 8, strong electrostatic repulsion between F-GCN and SMZ^- significantly reduces photocatalytic removal (87% at pH 9, 82.5% at pH 11).

Influence of pollutant concentration. The degradation efficiency of both antibiotics decreases with increasing initial concentrations. Specifically, with the antibiotic concentration rising from 5 mg L^{-1} to 20 mg L^{-1}, the degradation rate dropped from 98.4% to 89.2% for OFC (Fig. 7d) and from 95.4% to 80% for SMZ (Fig. 7e). This decline can be

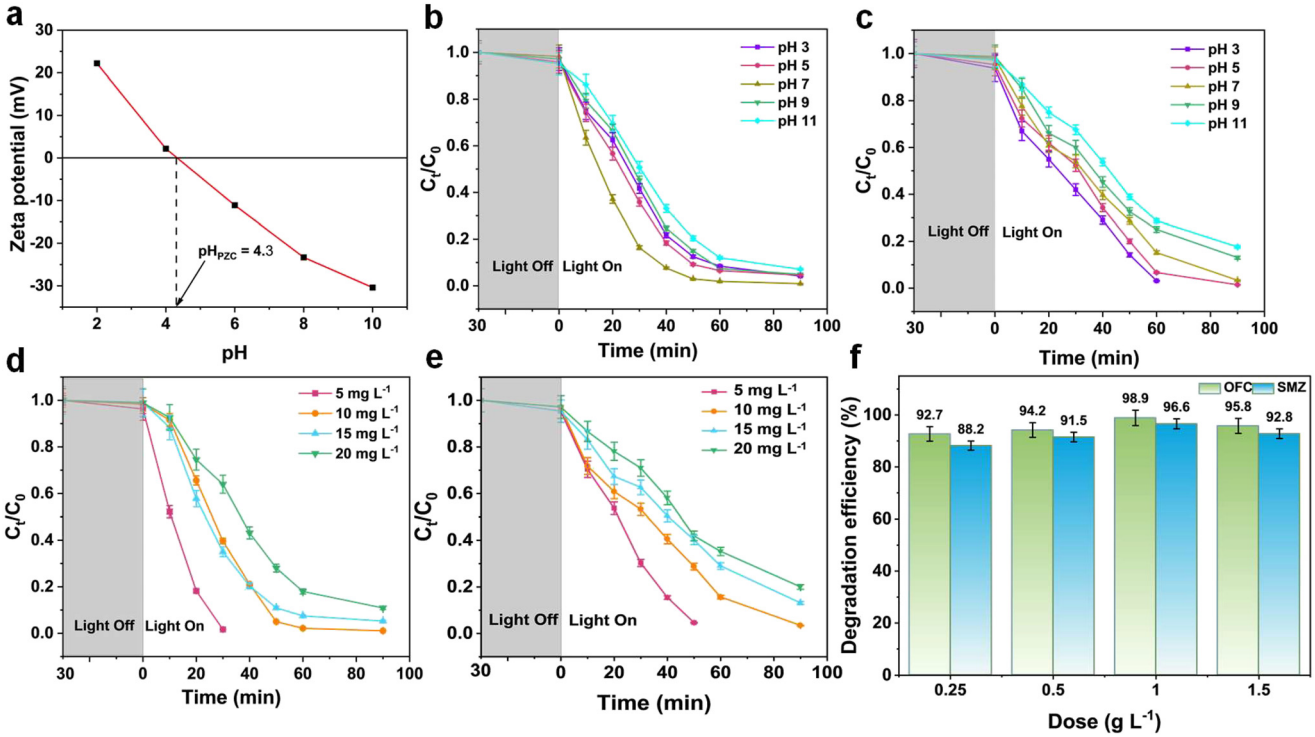

Fig. 7 (a) Zeta potential of F-GCN as a function of pH and point of zero charge (pH$_p$zc). Effects of initial solution pH on the photocatalytic degradation of (b) OFC and (c) SMZ (experimental conditions: C_0 = 10 mg L^{-1}; photocatalyst dose = 1 g L^{-1}; temperature = 25 °C). Effects of initial reactant concentration on the degradation of (d) OFC and (e) SMZ (experimental conditions: photocatalyst dose = 1 g L^{-1}; temperature = 25 °C). (f) Effects of photocatalyst dosage on the degradation of OFC and SMZ (experimental conditions: C_0 = 10 mg L^{-1}; temperature = 25 °C).

attributed to the relatively constant ROS generation under fixed photocatalyst dose and irradiation conditions. At higher pollutant concentrations, the available ROS become insufficient to sustain complete degradation. Furthermore, increased levels of antibiotics produce more intermediate species, which compete with the parent molecules for active sites on F-GCN, collectively reducing photocatalytic efficiency.

Effect of the catalyst dose. The photocatalyst dosage exerts a significant influence on pollutant degradation efficiency. Increasing the F-GCN concentration from 0.25 to 1 g L^{-1} enhanced the degradation of OFC from 92.7% to 98.9% and the degradation of SMZ from 88.2% to 96.6% within 90 min (Fig. 7f). This improvement can be attributed to the increased availability of active catalytic sites and the generation of larger quantities of ROS, which collectively accelerate antibiotic degradation. However, when the catalyst loading was further increased to 1.5 g L^{-1}, the degradation efficiency decreased to 95.8% for OFC and 92.8% for SMZ. This decline is likely due to excessive catalyst concentration, leading to particle agglomeration and inhomogeneous dispersion, which reduces the effective surface area and attenuates incident light through photon absorption and scattering. Moreover, excessive catalyst loading can hinder light penetration and limit charge carrier generation, thereby lowering the overall photocatalytic activity.

Effect of common inorganic anions and cations. In real water matrices, various inorganic ions can influence photocatalyst performance by altering the solution pH, scavenging free radicals, or blocking active catalytic sites. The effects of different anions on the photocatalytic degradation of OFC and SMZ by F-GCN are illustrated in Fig. 8a and b, respectively. Compared to OFC, the presence of inorganic anions in the SMZ reaction medium exhibited a more pronounced inhibitory effect on photocatalytic degradation (Fig. 8b). Specifically, the inhibitory effect of anions on SMZ degradation followed the order: nitrate (NO_3^-) < chloride (Cl^-) < hydrogen phosphate (HPO_4^{2-}) < carbonate (CO_3^{2-}) < sulfate (SO_4^{2-}), whereas for OFC, the milder inhibitory effect increased in the order: NO_3^- < CO_3^{2-} < HPO_4^{2-} < SO_4^{2-} < Cl^-. Although NO_3^- can quench photogenerated electrons and holes to produce radicals with weaker oxidation capacity, its interference in the degradation of both antibiotics is minimal. This is likely because NO_3^- interacts weakly with the photocatalyst and neither significantly alters the solution pH nor effectively competes with antibiotics for active sites on F-GCN. The inhibition caused by Cl^- ions can be attributed to the formation of less reactive Cl_2 species, as well as to the reaction of Cl^- with generated ROS to yield halogenated intermediates of lower oxidative potential. The strong inhibition of SMZ degradation by SO_4^{2-} is primarily due to its ability to scavenge holes and electrons, forming $^{\bullet}SO_4^-$ radicals, which possess a lower oxidation potential than the primary oxidants. In contrast, the slightly weaker impact of SO_4^{2-} on OFC removal is likely associated with the pH-

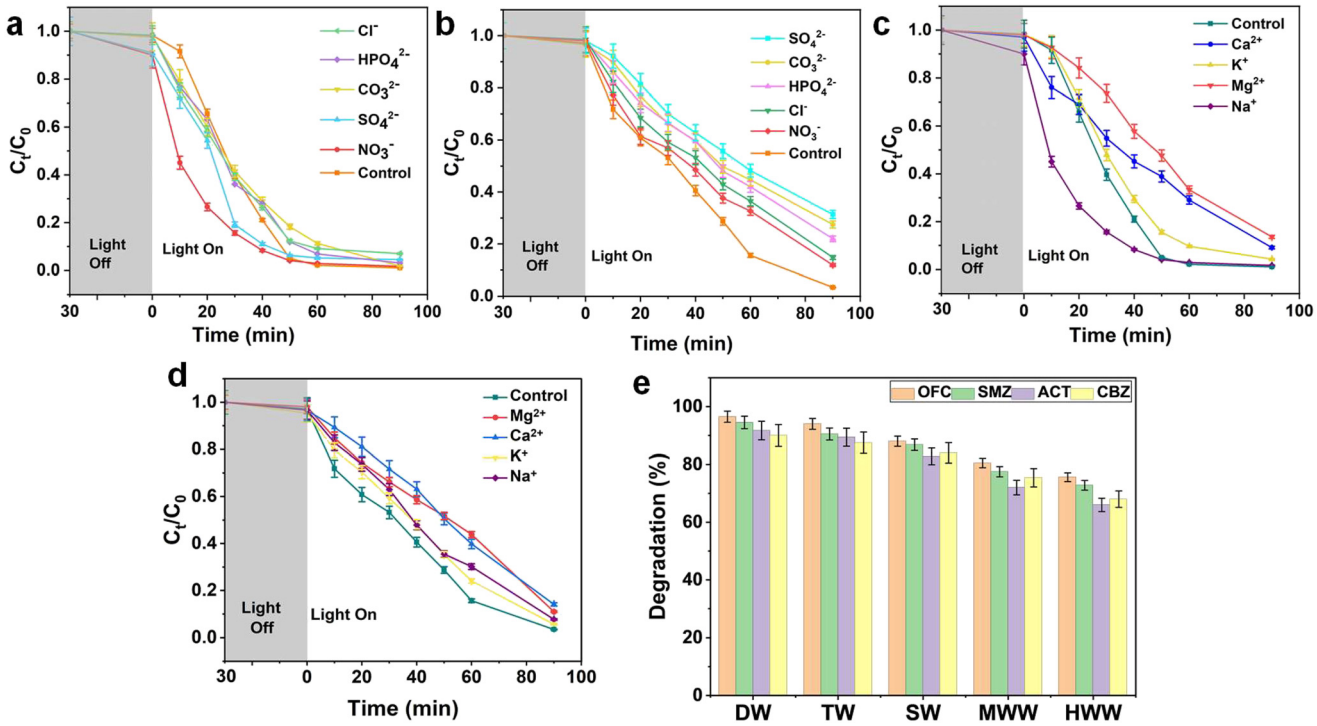

Fig. 8 Photocatalytic degradation of (a) OFC and (b) SMZ in the presence of anions, and (c) OFC and (d) SMZ in the presence of cations over F-GCN under visible light irradiation (experimental conditions: C_0 = 10 mg L^{-1}; photocatalyst dose = 1 g L^{-1}; anion/cation concentration = 20 mM; temperature = 25 °C). (e) Effect of different water matrices on the photocatalytic degradation of a quaternary mixture of OFC, SMZ, ACT, and CBZ over F-GCN (experimental conditions: C_0 = 10 mg L^{-1}; photocatalyst dose = 1 g L^{-1}; temperature = 25 ± 2 °C).

dependent reactivity of $^{\bullet}SO_4^-$.[38] Similarly, HPO_4^{2-} and CO_3^{2-} can both scavenge holes and $^{\bullet}OH$ radicals, generating less reactive species while simultaneously increasing the alkalinity of the reaction medium. These combined effects significantly reduce the photocatalytic degradation efficiency of both SMZ and OFC over F-GCN. On the other hand, inorganic cations such as sodium (Na^+), potassium (K^+), calcium (Ca^{2+}), and magnesium (Mg^{2+}) exert a minor negative influence on the degradation rates of both antibiotics (Fig. 8c and d), likely due to electrostatic interaction between the negatively charged F-GCN surface (at the studied pH) and these metal cations. Likely, these cations can adsorb onto the photocatalyst surface, hindering antibiotic molecules from accessing the catalytically active sites of F-GCN, which in turn reduces the overall removal efficiency.

Effect of real water matrices on the removal of antibiotic cocktails. To evaluate the robustness of the photocatalyst under environmentally relevant conditions, its performance was further assessed in different natural and wastewater samples. Accordingly, the practical applicability of F-GCN was examined by treating a mixed solution of various pharmaceutically active compounds, including antibiotics (SMZ, OFC), an antiepileptic (CBZ), and an analgesic (ACT), across five distinct water matrices (Fig. 8e). Compared with its performance in deionized water, the photocatalytic activity exhibited a slight decline in TW and SW, primarily due to the scavenging of ROS by anionic impurities that compete with target pollutants for oxidizing species. Nevertheless, despite such competitive inhibition, F-GCN maintained an average treatment efficiency exceeding 80% in potable water matrices.

In contrast, a more pronounced reduction in photocatalytic efficiency was observed in wastewater samples, likely due to the higher levels of organic matter, inorganic anions, turbidity, and total dissolved solids (Table S4). Natural organic matter containing phenolic and carboxyl groups can suppress ROS formation and block active catalytic sites, thereby impeding pollutant degradation. Additionally, background organic constituents compete with antibiotics for active radicals and generate intermediate products that further neutralize ROS. Collectively, these effects hinder photocatalytic degradation in both MWW and HWW by scavenging reactive species, altering pH, reducing light penetration, and obstructing active sites on F-GCN.

To mitigate these challenges and enable large-scale deployment of the developed F-GCN photocatalyst, appropriate pretreatment strategies may be employed to minimize the influence of dissolved organic matter and coexisting ions. Typical approaches include coarse filtration (*e.g.*, 0.45 μm membrane filtration) to remove suspended particulates, coagulation–flocculation using conventional coagulants such as alum or ferric salts to reduce dissolved organic carbon, and low-cost adsorption processes (*e.g.*, activated carbon or biochar) to further eliminate interfering species prior to photocatalytic treatment. Furthermore, operational optimizations, including adjusting catalyst dosage, extending irradiation time, or tuning solution pH to enhance charge separation and pollutant

adsorption, can further improve degradation efficiency in complex water matrices.

3.2.3 Identification of reaction intermediates and degradation pathways. To elucidate the mechanistic pathway of visible light-driven antibiotic degradation over F-GCN, transient intermediates and transformation products were identified using LCMS spectra, as shown in Fig. S5 and S6. Based on the existing literature and detailed analysis of these molecular structures, a plausible degradation pathway for OFC is proposed in Fig. 9. The mass peak at m/z = 362 corresponds to intact OFC, from which four primary degradation pathways (A–D) were identified. In pathway A, oxidation and hydroxyl substitution of the methyl group on the piperazine ring yield intermediate O1 (m/z = 364), followed by C–C bond cleavage to form O2 (m/z = 350).[39,40] Pathway B involves partial demethylation by ROS to generate O3 (m/z = 349), which undergoes further demethylation and decarboxylation to produce O4 (m/z = 290).[36,41] In pathway C, cleavage of the piperazine ring and partial fragmentation of the quinoline moiety initially give rise to O5 (m/z = 175), which is further oxidized to O6 (m/z = 149).[42,43] Pathway D begins with the removal of the piperazine moiety, forming O7 (m/z = 251), which undergoes ROS-induced defluorination to O8 (m/z = 235) and partial deamination to yield O9 (m/z = 189).[42] Regardless of the pathway, all intermediates are progressively degraded into smaller compounds, including O10 (m/z = 127), O11 (m/z = 87), and O12 (m/z = 73), and ultimately mineralized into carbon dioxide (CO_2), water (H_2O), fluoride (F^-), NO_3^-, and ammonium (NH_4^+) ions.

Similarly, the photocatalytic degradation of SMZ over F-GCN proceeds *via* oxidative reactions, including hydroxylation and cleavage of C–N, S–N, and N–O bonds, producing simpler intermediates (Fig. 10). The dominant peak at m/z = 254 corresponds to intact SMZ. In pathway A, ROS-induced S–N bond cleavage generates P1 (m/z = 98) and P2 (m/z = 156).[28,36] Pathway B involves C–N bond cleavage by $^{\bullet}O_2^-$ to form P3 (m/z = 171), which subsequently undergoes ring opening to yield P4 (m/z = 118).[36] In pathway C, S–C bond cleavage produces P5 (m/z = 99) and aniline (P6, m/z = 94), with P6 further hydroxylated to P7 (m/z = 110).[44] Pathway D involves oxidation of the benzene-linked amine, forming nitroso-SMX (P8, m/z = 268), which undergoes further hydroxylation and bond cleavage to yield P9 (m/z = 99) and P10 (m/z = 155).[45] Additionally, electrophilic modification of the isoxazole ring produces P11 (m/z = 274), which is cleaved into P12 (m/z = 135) and P13 (m/z = 110).[28] All intermediates are ultimately degraded into smaller hydrocarbons (P14–P17, m/z = 74–119) and mineralized to CO_2 and H_2O, with the nitrogen from SMZ oxidized to NH_4^+ and NO_3^- ions.

3.2.4 Reusability study. The reusability of F-GCN for the treatment of antibiotic-contaminated water was evaluated

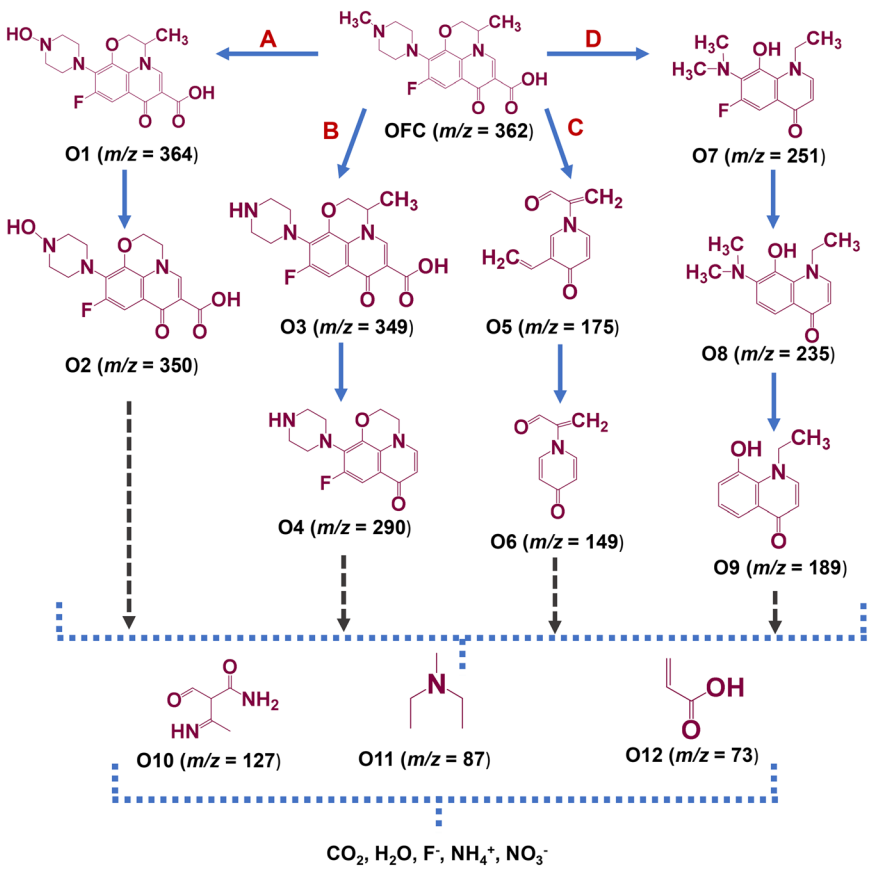

Fig. 9 Proposed photocatalytic degradation pathways of OFC over F-GCN under visible light irradiation.

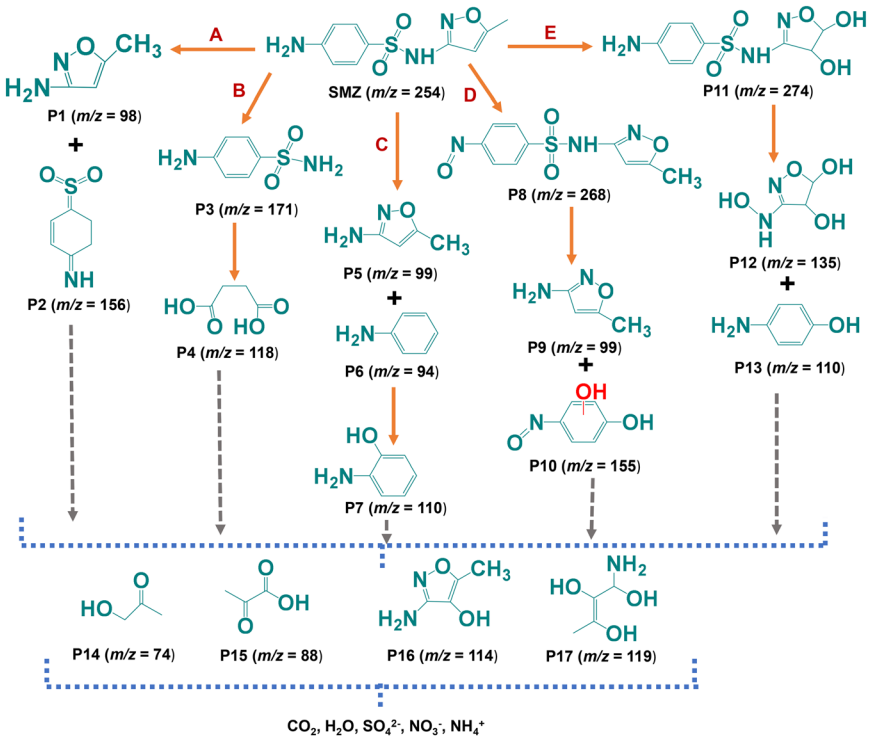

Fig. 10 Plausible routes for the photocatalytic degradation of SMZ over F-GCN under visible light irradiation.

over multiple cycles of filtration, washing, and drying. As depicted in Fig. 11a and b, the catalyst maintained high activity, with OFC and SMZ degradation efficiencies of 91.9% and 88.5%, respectively, even after three consecutive reuse

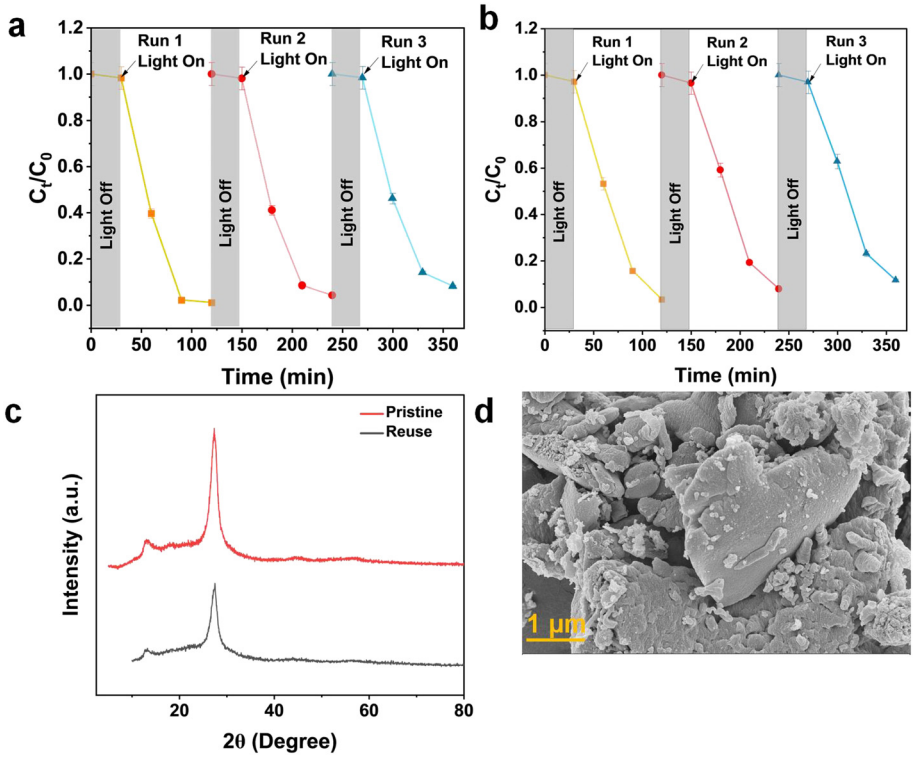

Fig. 11 Reusability of F-GCN for the photocatalytic degradation of (a) OFC and (b) SMZ over three cycles. (c) Comparison of the XRD patterns of F-GCN before and after three photocatalytic cycles, and (d) FEG-SEM image of F-GCN after three photocatalytic cycles.

cycles, demonstrating excellent stability and recoverability. The slight reduction in performance is likely due to co-adsorption of OFC, SMZ, or their by-products on the catalyst surface, as well as minor loss of active sites. Structural integrity was confirmed by XRD analysis (Fig. 11c), which showed that the crystalline framework of F-GCN remained unchanged after repeated use. Moreover, FEG-SEM images of the reused catalyst (Fig. 11d) revealed no significant morphological alterations, further corroborating its robustness over multiple cycles. Moreover, fluoride leaching from F-GCN was evaluated by ion chromatography (Dionex ICS-2100, Thermo Scientific) after three consecutive photocatalytic cycles. The leached F^- concentration was found to be below 0.1 mg L^{-1}, well below the WHO guideline limit for drinking water (1.5 mg L^{-1}), confirming the structural stability and environmental safety of the catalyst.

3.2.5 Toxicity of the photocatalysis end-products. The photocatalytic degradation of OFC and SMZ using F-GCN generates various low-molecular-weight intermediates and by-products, which could potentially pose environmental risks if released. To evaluate the toxicity of the final degradation products, bacterial colony-forming units (CFUs) were counted in both untreated and treated antibiotic solutions using triplicate experiments (Fig. 12). As expected, untreated OFC and SMZ solutions strongly inhibited *E. coli* growth due to their antimicrobial activity. In contrast, the photocatalytic degradation products exhibited no detrimental effect on *E. coli* survival. Additionally, CFU counts for the treated solutions were comparable to those in deionized water (Table S5), indicating that the F-GCN photocatalytic process effectively eliminates the antibacterial properties of OFC and SMZ.

To further assess the ecological impact of the transformation products, their phytotoxicity was evaluated using Indian mung bean seed germination and growth, as seed germination is highly sensitive to chemical exposure (Table S6). Experiments were conducted under three conditions: deionized water (control), treated antibiotic solution, and untreated antibiotic solution. Control seeds exhibited healthy growth, with 74 ± 3.1% germination and ~6 cm root-shoot length for OFC, and 80 ± 3.4% germination and ~7 cm root-shoot length for SMZ. Seeds exposed to treated solutions showed similar results (67 ± 2.8% germination for OFC and 74 ± 2.5% for SMZ), indicating effective detoxification without harmful intermediates. In contrast, untreated OFC and SMZ markedly reduced germination (27 ± 2.3% for OFC and 34 ± 1.9% for SMZ), stunted root-shoot growth (~2.5–3 cm), and caused visible stress symptoms, confirming that photocatalysis substantially mitigates the phytotoxicity of these antibiotics.

4. Conclusion

In summary, various non-metal-doped GCN photocatalysts were successfully synthesized *via* a one-step thermal co-condensation reaction, demonstrating that elemental doping can effectively tailor their structural, electronic, and optical properties for enhanced visible light-driven photocatalysis. Specifically, incorporation of B, S, P, or F atoms into the GCN framework modulates the band structure, improves charge separation, and broadens light absorption, leading to superior photocatalytic degradation of two broad-spectrum antibiotics, OFC and SMZ, in aqueous solutions under 90

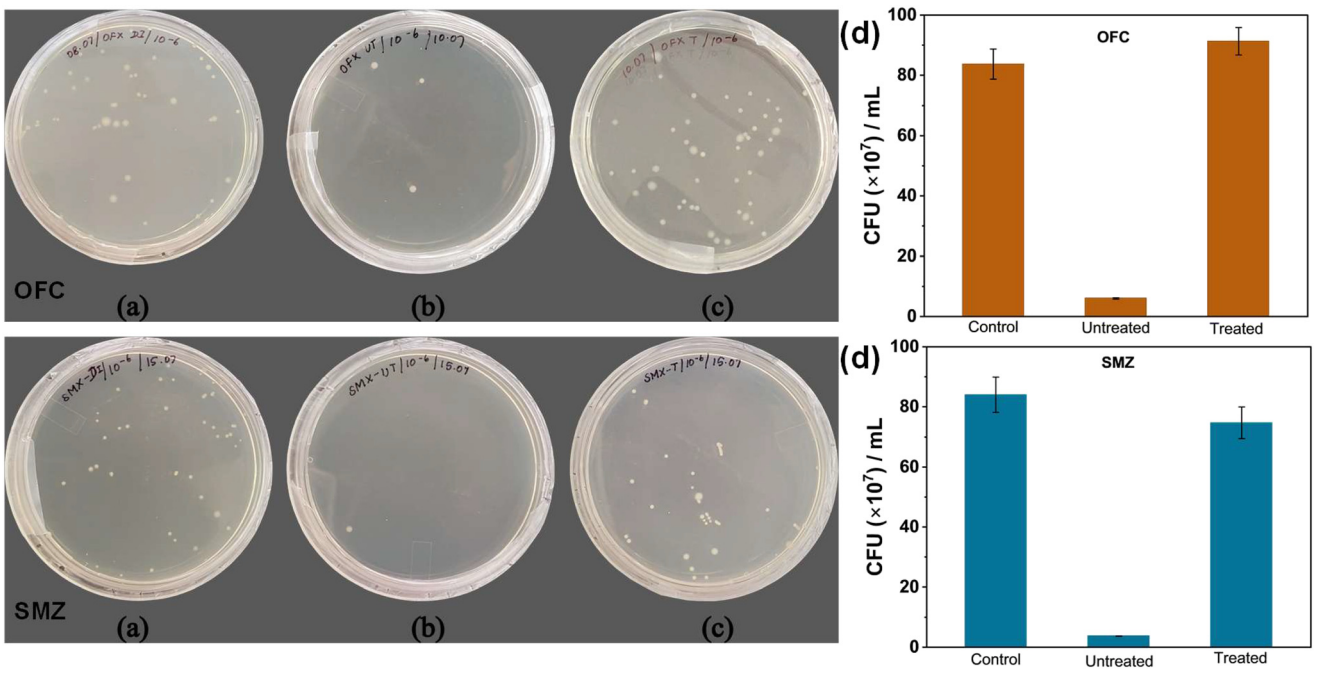

Fig. 12 Toxicity evaluation of (b) untreated and (c) treated OFC and SMZ solution toward *E. coli* with respect to (a) deionized water (control). (d) Viability of bacterial cells (in CFU mL^{-1}) in treated and untreated OFC and SMZ aqueous solution with respect to the control.

min of visible light irradiation compared to pristine GCN. Among these, F-GCN exhibited the best performance (98.9% for OFC and 96.5% for SMZ), attributed to semi-ionic C–F bonds that promote charge separation and migration, a high mesoporous surface area providing abundant active sites, and lattice distortion facilitating n–π* transitions, along with a reduced band gap (2.74 eV), enhancing visible light absorption. Mechanistic studies revealed that the synergistic action of holes and $^{\bullet}O_2^-$ radicals drive the photocatalytic degradation of OFC and SMZ. The treatment of a quaternary mixture of antibiotics, analgesics, and antiepileptics in different real water matrices further confirmed the promising practical applicability of F-GCN, although pretreatment to remove interfering compounds is recommended for optimal performance. Importantly, bacterial colony counts and seed germination assays demonstrated that the final degradation products pose minimal ecological risk. Overall, non-metal doping provides a versatile strategy to optimize GCN-based photocatalysts, paving the way for their use in efficient and sustainable water purification technologies.

Author contributions

Debanjali Dey: writing – original draft, methodology, investigation, formal analysis, data curation, and conceptualization. Shamik Chowdhury: writing – review & editing, validation, supervision, resources, funding acquisition, and formal analysis. Ramkrishna Sen: writing – review & editing and supervision.

Conflicts of interest

The authors declare that they have no known competing financial interests or personal relationships that could have appeared to influence the work reported in this paper.

Data availability

Data will be made available upon request. Supplementary information (SI) is available. See DOI: https://doi.org/10.1039/d5en00771b.

Acknowledgements

This work was financially supported by the Department of Science and Technology (DST), Government of India through its Solar Energy Research and Development (SERD) initiative (File No. DST/TMD/CERI/RES/2020/41). Debanjali Dey is thankful for the financial support provided by the Ministry of Education, Government of India through its Prime Minister's Research Fellowship scheme for her doctoral study.

References

1 M. Patel, R. Kumar, K. Kishor, T. Mlsna, C. U. Pittman and D. Mohan, Pharmaceuticals of emerging concern in aquatic systems: chemistry, occurrence, effects, and removal methods, *Chem. Rev.*, 2019, **119**, 3510–3673, DOI: 10.1021/acs.chemrev.8b00299.

2 P. Barathe, K. Kaur, S. Reddy, V. Shriram and V. Kumar, Antibiotic pollution and associated antimicrobial resistance in the environment, *J. Hazard. Mater. Lett.*, 2024, **5**, 100105, DOI: 10.1016/j.hazl.2024.100105.

3 B. C. Hodges, E. L. Cates and J.-H. Kim, Challenges and prospects of advanced oxidation water treatment processes using catalytic nanomaterials, *Nat. Nanotechnol.*, 2018, **13**, 642–650, DOI: 10.1038/s41565-018-0216-x.

4 J. Luo, J. Chen, X. Chen, X. Ning, L. Zhan and X. Zhou, Construction of cerium oxide nanoparticles immobilized on the surface of zinc vanadate nanoflowers for accelerated photocatalytic degradation of tetracycline under visible light irradiation, *J. Colloid Interface Sci.*, 2021, **587**, 831–844, DOI: 10.1016/j.jcis.2020.11.044.

5 S. Li, X. Li, Y. Liu, P. Zhang, J. Zhang and B. Zhang, Interfacial engineering of a plasmonic $Ag/Ag_2CO_3/C_3N_5$ S-scheme heterojunction for high-performance photocatalytic degradation of antibiotics, *Chin. J. Catal.*, 2025, **72**, 130–142, DOI: 10.1016/S1872-2067(25)64652-3.

6 S. Li, C. You, K. Rong, C. Zhuang, X. Chen and B. Zhang, Chemically bonded Mn0.5Cd0.5S/BiOBr S-scheme photocatalyst with rich oxygen vacancies for improved photocatalytic decontamination performance, *Adv. Powder Mater.*, 2024, **3**, 100183, DOI: 10.1016/j.apmate.2024.100183.

7 R. Xu, J. Li, G. Sui, Y. Zhuang, D. Guo, Z. Luo, S. Liang, H. Yao, C. Wang and S. Chen, Constructing supramolecular self-assembled porous $g\text{-}C_3N_4$ nanosheets containing thiophene-groups for excellent photocatalytic performance under visible light, *Appl. Surf. Sci.*, 2022, **578**, 152064, DOI: 10.1016/j.apsusc.2021.152064.

8 A. Ali, M. Shoeb, B. Li and M. A. Khan, Photocatalytic degradation of antibiotic drug and dye pollutants under visible-light irradiation by reduced graphene oxide decorated MoO_3/TiO_2 nanocomposite, *Mater. Sci. Semicond. Process.*, 2022, **150**, 106974, DOI: 10.1016/j.mssp.2022.106974.

9 S. Kar, T. Pal and S. Ghosh, Removal of norfloxacin from wastewater by adsorption onto SnS_2 followed by photocatalytic degradation, *ChemistrySelect*, 2023, **8**, e202300878, DOI: 10.1002/slct.202300878.

10 M. S. Shruti, A. Sasmal, H. HyukSu and A. K. Nayak, Facile synthesis of N-doped V_2O_5@ $g\text{-}C_3N_4$ electrodes for enhanced symmetric supercapacitor application, *Mater. Chem. Phys.*, 2024, **314**, 128826, DOI: 10.1016/j.matchemphys.2023.128826.

11 X. Wang, S. Blechert and M. Antonietti, Polymeric graphitic carbon nitride for heterogeneous photocatalysis, *ACS Catal.*, 2012, **2**, 1596–1606, DOI: 10.1021/cs300240x.

12 S. Chandrappa, S. J. Galbao, A. Furube and D. H. K. Murthy, Extending the optical absorption limit of graphitic carbon nitride photocatalysts: a review, *ACS Appl. Nano Mater.*, 2023, **6**, 19551–19572, DOI: 10.1021/acsanm.3c04740.

13 L. Chen, M. A. Maigbay, M. Li and X. Qiu, Synthesis and modification strategies of $g\text{-}C_3N_4$ nanosheets for photocatalytic applications, *Adv. Powder Mater.*, 2024, **3**, 100150, DOI: 10.1016/j.apmate.2023.100150.

14 X. Cao, J. Shen, X.-F. Li and Y. Luo, Spin polarization-induced facile dioxygen activation in boron-doped graphitic carbon nitride, *ACS Appl. Mater. Interfaces*, 2020, **12**, 52741–52748, DOI: 10.1021/acsami.0c16216.

15 S. Li, R. Li, K. Dong, Y. Liu, X. Yu, W. Li, T. Liu, Z. Zhao, M. Zhang, B. Zhang and X. Chen, Self-floating $Bi_4O_5Br_2$/P-doped C_3N_4/carbon fiber cloth with S-scheme heterostructure for boosted photocatalytic removal of emerging organic contaminants, *Chin. J. Catal.*, 2025, **76**, 37–49, DOI: 10.1016/S1872-2067(25)64780-2.

16 M. Chen, M. Guo, M. Zhai, J. Xu and L. Wang, Manipulating electronic structure and light absorption of carbon nitride via P-doping and local crystallization for efficient photocatalytic reduction of CO_2, *J. CO_2 Util.*, 2023, **68**, 102392, DOI: 10.1016/j.jcou.2023.102392.

17 Z. Li, Q. Chen, Q. Lin, Y. Chen, X. Liao, H. Yu and C. Yu, Three-dimensional P-doped porous g-C_3N_4 nanosheets as an efficient metal-free photocatalyst for visible-light photocatalytic degradation of Rhodamine B model pollutant, *J. Taiwan Inst. Chem. Eng.*, 2020, **114**, 249–262, DOI: 10.1016/j.jtice.2020.09.019.

18 H. Guo, Z. Shu, D. Chen, Y. Tan, J. Zhou, F. Meng and T. Li, One-step synthesis of S-doped g-C_3N_4 nanosheets for improved visible-light photocatalytic hydrogen evolution, *Chem. Phys.*, 2020, **533**, 110714, DOI: 10.1016/j.chemphys.2020.110714.

19 L. Li, M. Chao, B. Zhang, C. Song, C. Luo and L. Yan, A sulfur-doped alga-like gC_3N_4 photocatalyst for enhanced photocatalytic and antimicrobial properties, *New J. Chem.*, 2024, **48**, 7845–7855, DOI: 10.1039/D4NJ00296B.

20 Y. Zhou, W. Lv, B. Zhu, F. Tong, J. Pan, J. Bai, Q. Zhou and H. Qin, Template-free one-step synthesis of g-C_3N_4 nanosheets with simultaneous porous network and S-doping for remarkable visible-light-driven hydrogen evolution, *ACS Sustainable Chem. Eng.*, 2019, **7**, 5801–5807, DOI: 10.1021/acssuschemeng.8b05374.

21 H. Wang, L. Yu, J. Jiang, Arramel and J. Zou, S-doping of the N-Sites of g-C_3N_4 to enhance photocatalytic H_2 evolution activity, *Acta Phys.-Chim. Sin.*, 2024, **40**, 2305047, DOI: 10.3866/PKU.WHXB202305047.

22 H. Zhan, Q. Zhou, M. Li, R. Zhou, Y. Mao and P. Wang, Photocatalytic O_2 activation and reactive oxygen species evolution by surface BN bond for organic pollutants degradation, *Appl. Catal., B*, 2022, **310**, 121329, DOI: 10.1016/j.apcatb.2022.121329.

23 I. Ullah, X. Lu, S. Chen, J. Li, S. Habib, G. Murtaza, T. Tofaz and A. Xu, Electron-deficient boron-doped g-C_3N_4 as an efficient and robust photocatalyst for visible-light driven hydrogen evolution from water splitting, *Adv. Sustainable Syst.*, 2024, **8**, 2400103, DOI: 10.1002/adsu.202400103.

24 H. Ye, Z. Wang, F. Yu, S. Zhang, K. Kong, X. Gong, J. Hua and H. Tian, Fluorinated conjugated poly (benzotriazole)/g-C_3N_4 heterojunctions for significantly enhancing photocatalytic H_2 evolution, *Appl. Catal., B*, 2020, **267**, 118577, DOI: 10.1016/j.apcatb.2019.118577.

25 B. L. Phoon, T. C.-K. Yang, B. F. Leo, C. W. Lai, S. W. Phang and J. C. Juan, Mesoporous semi-ionic F-doped g-C_3N_4 as efficient photocatalyst for tetracycline removal under visible light, *Environ. Technol. Innovation*, 2023, **32**, 103303, DOI: 10.1016/j.eti.2023.103303.

26 H. Liu, X. Wang, H. Xu and C. Luo, Facile synthesis of F-doped g-C_3N_4/$Bi_2Fe_4O_9$ heterostructure with Z-scheme for enhanced photocatalytic performance in NO oxidation, *J. Phys. Chem. Solids*, 2020, **146**, 109500, DOI: 10.1016/j.jpcs.2020.109500.

27 Z. Chen, W. Chen, G. Liao, X. Li, J. Wang, Y. Tang and L. Li, Flexible construct of N vacancies and hydrophobic sites on g-C_3N_4 by F doping and their contribution to PFOA degradation in photocatalytic ozonation, *J. Hazard. Mater.*, 2022, **428**, 128222, DOI: 10.1016/j.jhazmat.2022.128222.

28 M. V. L. Gnanaguru, M. M. Ghangrekar and S. Chowdhury, 2D–2D g-C_3N_4/WS_2 Z-scheme heterojunction: Comparison of the photocatalytic degradation of tetracycline and sulfamethoxazole, *J. Photochem. Photobiol., A*, 2024, **456**, 115818, DOI: 10.1016/j.jphotochem.2024.115818.

29 F. Wang, Z. Zhu and J. Guo, 2D–2D ZnO/N doped gC_3N_4 composite photocatalyst for antibiotics degradation under visible light, *RSC Adv.*, 2021, **11**, 35663–35672, DOI: 10.1039/D1RA06607B.

30 Y. Dai, S. Cai, L. Wu, W. Yang, J. Xie, W. Wen, J.-C. Zheng and Y. Zhu, Surface modified CF x cathode material for ultrafast discharge and high energy density, *J. Mater. Chem. A*, 2014, **2**, 20896–20901, DOI: 10.1039/C4TA05492J.

31 D. Ma, Q. Xue, Y. Liu, F. Liang, W. Li, T. Liu, C. Zhuang, Z. Zhao and S. Li, Manipulating interfacial charge redistribution in Mn0.5Cd0.5S/N-rich C3N5 S-scheme heterojunction for high-performance photocatalytic removal of emerging contaminants, *J. Mater. Sci. Technol.*, 2026, **243**, 265–274, DOI: 10.1016/j.jmst.2025.05.011.

32 C. You, X. Zhang, Y. Zhao, R. Yan, Y. Shen, Q. Xue, W. Li, T. Liu, J. Jiang, X. Chen and S. Li, Plasmonic effect augmented S-scheme mechanism in $Ag/Ag_2O/C_3N_5$ photocatalyst enables efficient photocatalytic degradation of antibiotics, *J. Mater. Sci. Technol.*, 2026, **242**, 64–74, DOI: 10.1016/j.jmst.2025.05.002.

33 X. Zheng, Q. Zhang, T. Chen, Y. Wu, J. Hao, C. Tan, P. Chen, F. Wang, H. Liu, W. Lv and G. Liu, A novel synthetic carbon and oxygen doped stalactite-like g-C_3N_4 for broad-spectrum-driven indometacin degradation, *J. Hazard. Mater.*, 2020, **386**, 121961, DOI: 10.1016/j.jhazmat.2019.121961.

34 L. Yu, X. Zhang, G. Li, Y. Cao, Y. Shao and D. Li, Highly efficient $Bi_2O_2CO_3$/BiOCl photocatalyst based on heterojunction with enhanced dye-sensitization under visible light, *Appl. Catal., B*, 2016, **187**, 301–309, DOI: 10.1016/j.apcatb.2016.01.045.

35 M. Machreki, T. Chouki, G. Tyuliev, M. Fanetti, M. Valant, D. Arčon, M. Pregelj and S. Emin, The role of lattice defects on the optical properties of TiO_2 nanotube arrays for synergistic water splitting, *ACS Omega*, 2023, **8**, 33255–33265, DOI: 10.1021/acsomega.3c00965.

36 S. Das, S. Kumar, S. Sarkar, D. Pradhan, C. S. Tiwary and S. Chowdhury, High entropy spinel oxide nanoparticles for visible light-assisted photocatalytic degradation of binary mixture of antibiotic pollutants in different water matrixes, *J. Mater. Chem. A*, 2024, **12**, 16815–16830, DOI: 10.1039/D4TA02294G.

37 Y. Nosaka and A. Y. Nosaka, Generation and detection of reactive oxygen species in photocatalysis, *Chem. Rev.*, 2017, **117**, 11302–11336, DOI: 10.1021/acs.chemrev.7b00161.

38 J. Herrera-Ordonez, The role of sulfate radicals and pH in the decomposition of persulfate in aqueous medium: A step towards prediction, *Chem. Eng. J. Adv.*, 2022, **11**, 100331, DOI: 10.1016/j.ceja.2022.100331.

39 Q. Shang, X. Liu, M. Zhang, P. Zhang, Y. Ling, G. Cui, W. Liu, X. Shi, J. Yue and B. Tang, Photocatalytic degradation of ofloxacin antibiotic wastewater using TS-1/C_3N_4 composite photocatalyst: Reaction performance optimisation and estimation of wastewater component synergistic effect by artificial neural network and genetic algorithm, *Chem. Eng. J.*, 2022, **443**, 136354, DOI: 10.1016/j.cej.2022.136354.

40 B. Xia, J. Yao, C. Han, Z. Zhang, X. Chen and Y. Fang, Degradation of ofloxacin by UVA-LED/TiO_2 nanotube arrays photocatalytic fuel cells, *Chem. Pap.*, 2018, **72**, 359–368, DOI: 10.1007/s11696-017-0285-6.

41 G. Peng, C. Qi, X. Wang, L. Zhou, Q. He, W. Zhou and L. Chen, Activation of peroxymonosulfate by calcined electroplating sludge for ofloxacin degradation, *Chemosphere*, 2021, **266**, 128944, DOI: 10.1016/j.chemosphere.2020.128944.

42 S. Das, M. Sanjay, S. Kumar, S. Sarkar, C. S. Tiwary and S. Chowdhury, Magnetically separable MnFeCoNiCu-based high entropy alloy nanoparticles for photocatalytic oxidation of antibiotic cocktails in different aqueous matrices, *Chem. Eng. J.*, 2023, **476**, 146719, DOI: 10.1016/j.cej.2023.146719.

43 S. Sharma and S. Basu, Visible-light-induced photocatalytic response of easily recoverable Mn_2O_3/SiO_2 monolith in centimeter-scale towards degradation of ofloxacin: performance evaluation and product analysis, *Chemosphere*, 2022, **307**, 135973, DOI: 10.1016/j.chemosphere.2022.135973.

44 M. Kohantorabi, G. Moussavi, P. Oulego and S. Giannakis, Radical-based degradation of sulfamethoxazole via UVA/PMS-assisted photocatalysis, driven by magnetically separable Fe_3O_4@ CeO_2@ BiOI nanospheres, *Sep. Purif. Technol.*, 2021, **267**, 118665, DOI: 10.1016/j.seppur.2021.118665.

45 X. Xia, L. Deng, L. Yang and Z. Shi, Facile synthesis of CoOOH@ MXene to activate peroxymonosulfate for efficient degradation of sulfamethoxazole: performance and mechanism investigation, *Environ. Sci. Pollut. Res.*, 2022, **29**, 52995–53008, DOI: 10.1007/s11356-022-19664-3.